1. Confirmation of Te filling in single-wall carbon nanotubes (SWCNTs)

Four types of CNTs are used as containers for Te filling, and all of them are purchased from Sigma-Aldrich. The detailed characterization is listed below:

(1) SWCNTs are produced by the CoMoCATTM catalyst chemical vapor deposition (CVD) process with diameters ranging from 0.7-1.3 nm, and the stated average diameter is to be 0.82 nm. The SWCNTs are provided in powder form with more than 99% as SWCNT.

(2) SWCNTs with average diameter of 1.3 nm, prepared by arc plasma jet method using Ni and Y as catalyst. The SWCNTs are supplied in powder form with very high purity (>99% as carbon nanotube).

(3) MWCNTs with median diameter of 2.5-3.0 nm, prepared by patented CoMoCAT synthesis process, and the CNT purity is larger than 94% measured by TGA.

(4) MWCNTs, the outer diameter is 6-10 nm and the length is 0.5-10 μm. They are prepared by arc ablation method with MWCNT basis around 30%.

All the CNTs were characterized using Raman spectroscopy as shown in **Supplementary Figure** 1.

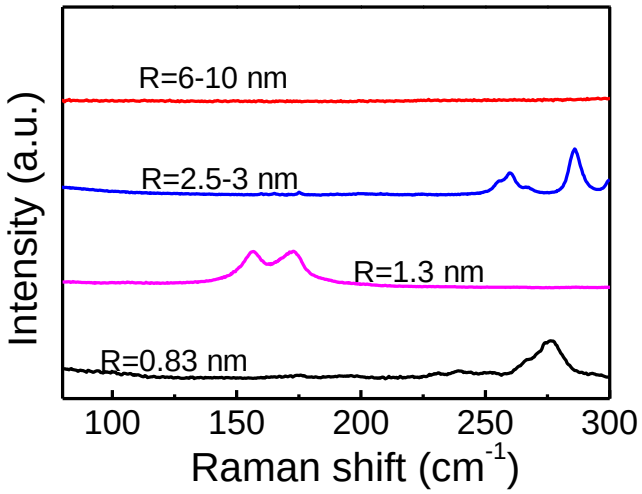

Supplementary Figure 1 | Raman spectrum of CNTs with the laser wavelength at 633 nm.

The SWCNT powder was first thermal treated at 500 ºC for 1h in air condition to open the tube ends, which enables the efficient filling of ultra-narrow Te NW. The as-grown Te-SWCNTs were ultrasonically dispersed in methanol solution and dropped on TEM microgrids for characterization. As the high-resolution TEM (HRTEM) image shown in **Supplementary Figure** 2, clear lattice fringe could be observed in the cavity of SWCNTs, indicating most of the SWCNTs were filled with Te NWs. The HAADF-STEM image could provide Z-contrast with atomic lateral resolution (Z =atomic number), by which we could determine the filling yield. Combined with a GIF Quantum spectrometer (Gatan) specialized for low-voltage operation and EDX mapping image of Te-SWCNTs (Inset image in **Supplementary Figure** 2b), we can determine that more than 90% of the SWCNTs were filled with Te atomic chains.

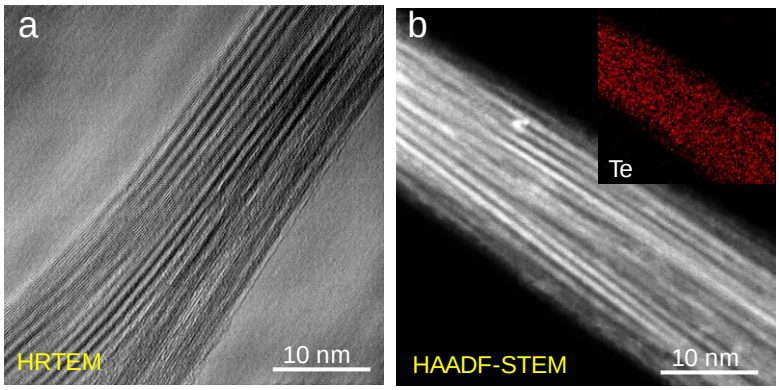

Supplementary Figure 2 | TEM characterization of Te chains in SWCNTs. **a,** HRTEM image. **b,** HAADF-STEM image. Inset shows the corresponding EDX mapping image.

The HAADF-STEM image could further demonstrate that the single Te atomic chain is inside the SWCNT. As shown in **Supplementary Figure** 3a, the 3-fold-symmetry helical coils of Te atoms can be clearly observed. In addition, larger Te NWs can be successfully obtained with the increase of CNT diameters (**Supplementary Figure 3b and 3c**). The results suggest that by carefully selecting the inner diameter of CNTs, controlling growth of ultra-narrow Te

NWs with few-number of atomic chains could be realized.

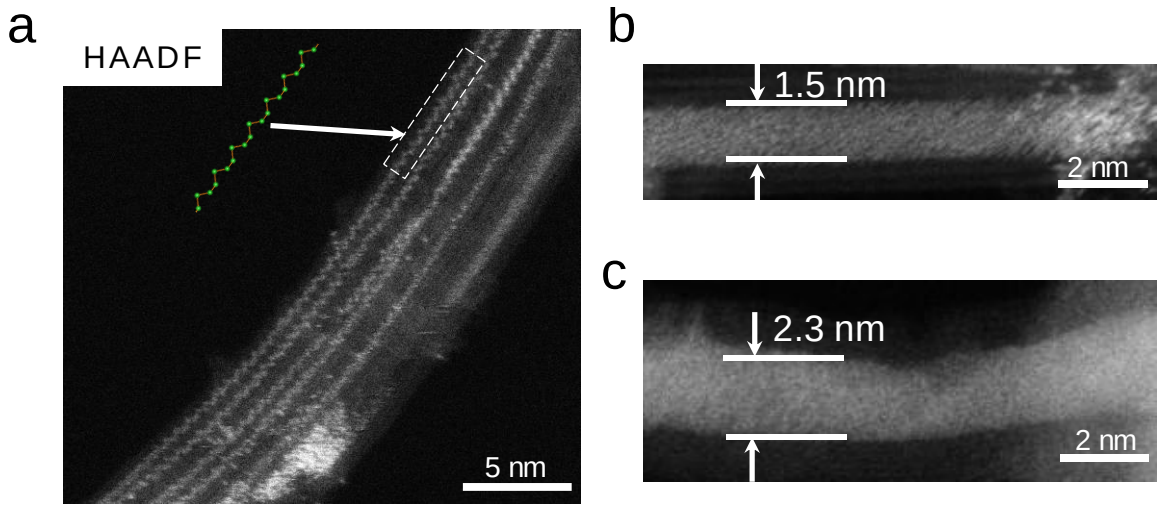

Supplementary Figure 3 | Characterization of ultra-narrow Te NWs isolated down to few-chain limit by CNT encapsulation. a, HAADF image of a single Te chain in 0.8 nm SWCNT, where the 3-fold-symmetry helical coils can be clearly distinguished. **b-c,** HAADF images of larger Te NWs in CNT with a diameter of 1.5 and 2.4 nm, respectively.

In the experiment, AFM was first used to locate the testing area where CNTs was sparsely distributed on the substrate. As shown in **Supplementary Figure 4a-c**, the individual SWCNTs could be clearly identified. The corresponding height profile and distribution statistics demonstrated that the outer diameter of SWCNTs ranges from 1.1-1.5 nm with the average value of 1.3 nm. In this way, the interference between SWCNTs towards the Raman vibration could be eliminated and the peak intensity of CNT radial breathing modes are greatly suppressed. **Supplementary Figure 4d** shows the corresponding Raman spectra of bare SWCNTs and Te-SWCNTs. By carefully eliminating the scattering information of SWCNTs, we can obtain the E_1 and A_1 peaks of single atomic Te chains, which locate at 83 cm^{-1} and 148 cm^{-1}, respectively, while the E_2 mode exhibits extremely small intensity. Note that the relative intensity ratio (E_1/A_1) of single Te atomic chains increases largely up to 1.1, much larger than that in bulk form (~0.26). It means the A_1 mode of single Te atomic chains is significantly

suppressed due to the SWCNT encapsulation.

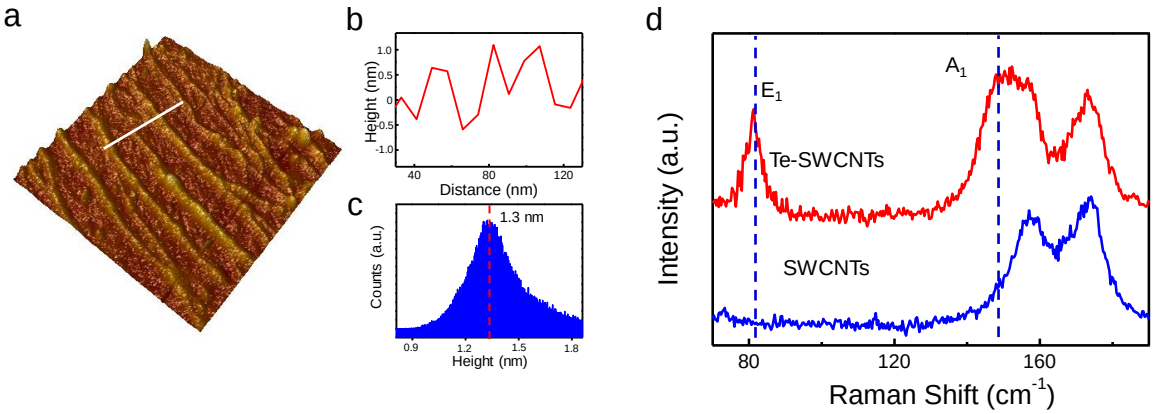

Supplementary Figure 4 | Raman characterization of Te atomic chains in SWCNT. a, 3D view of SWCNTs sparsely distributed on substrate. **b-c,** the corresponding height profile and distribution statistics of SWCNTs. **d,** The Raman spectra of bare SWCNTs and Te-SWCNTs.

The Raman spectrum obtained from single Te chains encapsulated in 0.8 nm SWCNTs shows only one strong peak at around 196 cm^{-1}, while other peaks are too weak to be detected (Supplementary Figure 5). This is understandable, since the energies of the A_1 and E_2 modes are closer, this significant change of the A_1 mode also impacts the energy and vibration of the E_2 mode and leads to the hybridization.

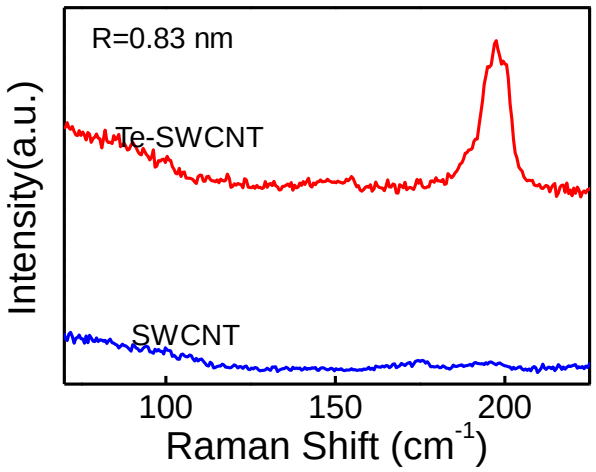

Supplementary Figure 5 | Raman characterization of single Te atomic chains in SWCNTs.

2. Photon energy calculation of Te atomic chain encapsulated in SWCNTs

As illustrated in Supplementary Figure 6a, free-standing single atomic Te chain was fully relaxed to obtain its photon energies [1-3]. DFT-relaxed structures give the frequency of E_1, E_2 and A_1 modes to be 68, 178 and 192 cm^{-1}, respectively. With the increase of chains, both the A_1 and E_2 would move toward the low-frequency direction, while the E_1 mode shows the opposite tendency, which are well matched with experiments. The DFT results suggest that vdW interaction between the Te chain and CNT is very weak and the CNT encapsulation keeps the free-standing structure of Te atomic chain.

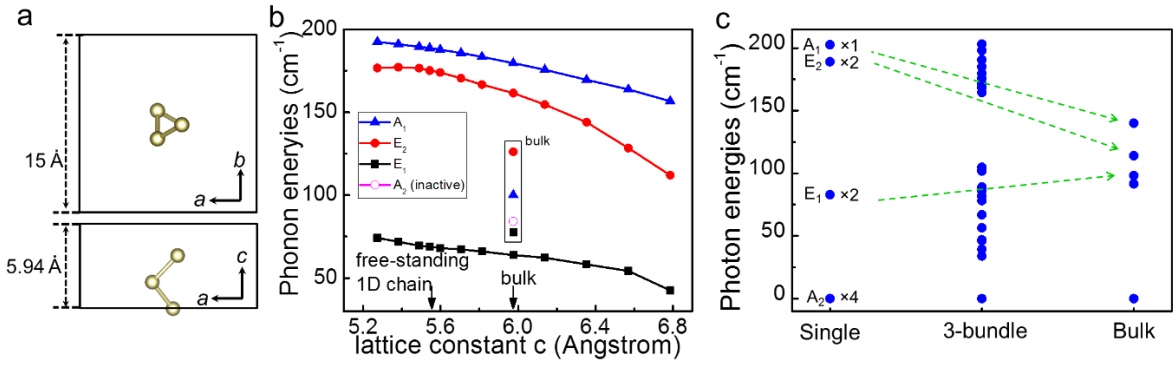

Supplementary Figure 6 | The photon energy calculation of Te atomic chains. a, Atomistic structure of the Te atomic chain. **b,** Phonon energies of a single atomic Te chain with dependence of lattice constant. **c,** Phonon energies for a single Te atomic chain and bulk Te. In 3-bundle case, the interaction between chains would split the Raman vibration modes and result into the increase of modes, while these modes are degenerated in single chain case or in bulk form.

It should be noted that defective 3H structure could be also energetically stable except for ideal 3H structure with SWCNT diameters larger than 1.1 nm. As shown in Supplementary Figure 7a, this screwed structure can be split into a possessing left- and another right-handed

chain. The corresponding electrical band structure and photon structure are present in Supplementary Figure 7b-c and Supplementary Figure 7e-f, respectively.

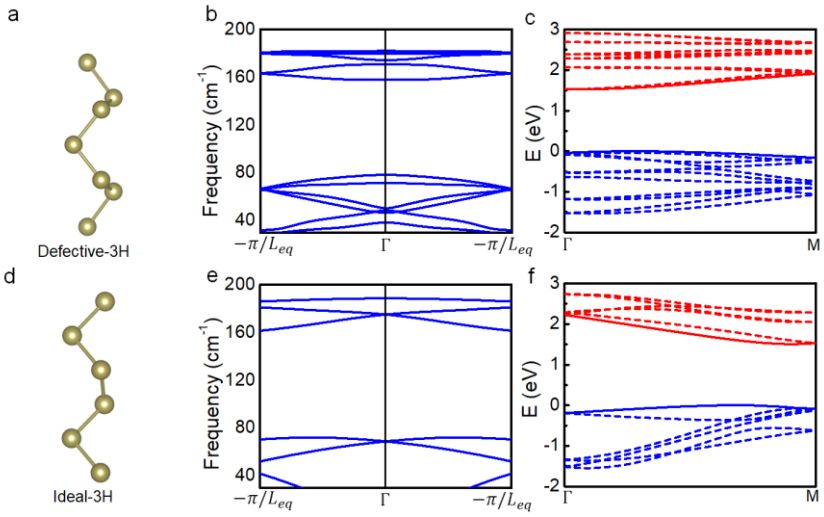

Supplementary Figure 7 | DFT calculation of defective 3H structure and ideal 3H structure. a, Atomistic structure of defective 3H structure. **b,** Corresponding phonon energies and **c,** electrical band structure. **d,** Atomistic structure of ideal 3H structure. **e,** Corresponding phonon energies and **f,** electrical band structure.

3. Ultra-narrow Te NWs shielded by BNNTs with different diameters.

BNNTs are obtained using chemical vapor deposition (CVD) combined with growth vapor trapping (GVT) approach as reported in our previous work[4] (Supplementary Figure 8). In the beginning, clean Si substrate was uniformly covered by 10 nm $MgCl_2$ films deposited by pulsed laser deposition (PLD) technique, and it was then placed upside down on the top of Al_2O_3 boat with B, $MgCl_2$, and FeO precursors (molar ratio of 4:1:1) and loaded at the end of a quartz tube. The quartz tube was placed in the center of a horizontal tube furnace with the holding temperature of 1200 ^oC for 30 min, and the ammonia flow was set to be 200 sccm. The

GVT is realized since the substrate is placed at the end of quartz tube, and the growth process cannot be affected by the flow of the ammonia gas.

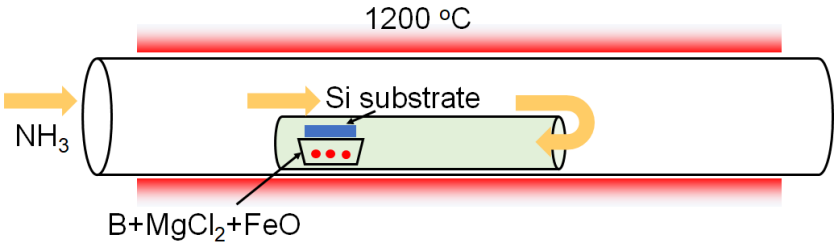

Supplementary Figure 8 | Experimental setup for the CVD growth of BNNTs.

Supplementary Figure 9 shows the scanning electron microscopy (SEM) image of the as-grown BNNTs on Si substrate, where clean and long BNNTs can be clearly observed, and the length is estimated to be longer than 10 μm. Transmission electron microscopy (TEM) indicates that these BNNTs exhibit a high-order tubular structure with uniform inner diameter along the axial direction (Supplementary Figure 9c). High-resolution TEM (Supplementary Figure 9d) demonstrates that the as-grown BNNTs are well crystallized almost without amorphous BN coatings on the surface of the sidewalls. Consist with previous results, the interlayer spacing of the BNNT walls is estimated as ~0.35 nm, suggesting the BNNT tends to crystalline with the (0001) faces along the radical direction. According to the distribution of inner diameter of BNNTs, we can confirm that these BNNTs have an average inner diameter of 5 nm (Supplementary Figure 9b).

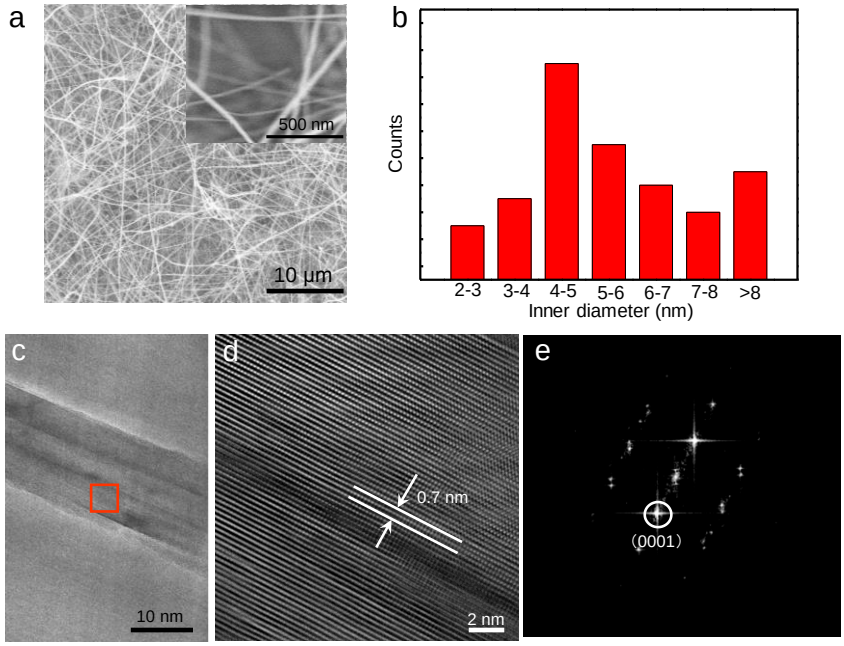

Supplementary Figure 9 | Materials characterization of BNNTs. a, SEM image of as-grown BNNTs on Si substrate. Inset image shows the enlarged SEM image. **b,** Statistics of the inner diameter of BNNTs. **c,** TEM of an individual BNNT showing nano-tubular structures of BNNTs with amorphous-free sidewalls. **d,** HRTEM of a BNNT with the interlayer distance to be 0.35 nm. **e,** Corresponding SEAD pattern of BNNT.

Chemical etching combined with thermal treatment was first utilized to open the ends of BNNTs, which ensures an efficient filling of Te NWs in the cavity of BNNTs. However, due to the strong interactions at Te/BNNT interface raised from the delocalization of π electrons in BNNTs, the high aspect ratio filling of Te is restricted, and only 50% of the BNNTs are successfully filled with Te NWs with the filling length less than 400 nm.

Te NW confined in BNNT would crystallize homogeneously in form of a single crystal. Supplementary Figure 10a shows the TEM characterization of an individual Te-BNNT, where the Te NW can be uniformly filled into the cavity of BNNT. Supplementary Figure 10b and 10c represent the HRTEM images of Te-BNNT obtained in the areas marked with red

rectangular in Supplementary Figure 10a. The lattice fringes belonged to Te NW can be clearly observed, suggesting that Te NW is well crystallized with high quality. The single-crystalline Te NW could be further confirmed by the corresponding SEAD pattern (inset image in the upright corner) collected from HTREM, where only single set of diffraction can be detected.

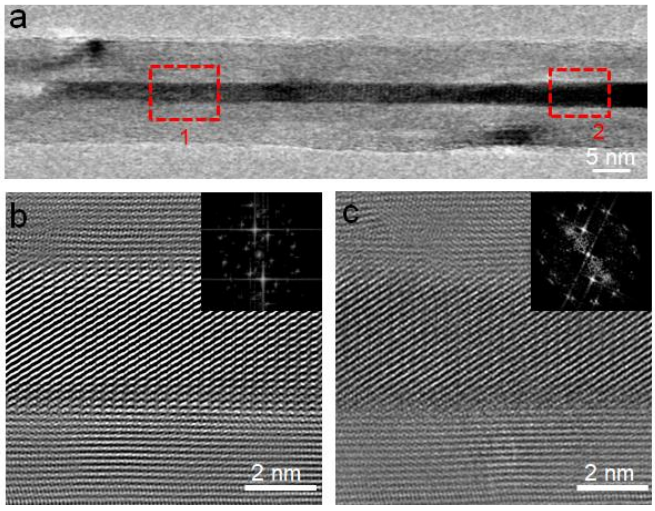

Supplementary Figure 10 | TEM characterization of Te-BNNT. a, low-magnificent TEM image of an individual Te NW encapsulated by BNNT. **b-c,** HRTEM images collected from the areas marked with rectangular in Supplementary Figure 10a. Inset image shows the corresponding SEAD patterns of single-crystalline Te NW.

The EDX mapping could strongly demonstrate that most of Te crystals are filled inside the BNNT instead of attached on the surface. As shown in Supplementary Figure 11a, no Te residuals could be detected on the outer surface of BNNT. In order to eliminating the influence of Te clusters, plasma treatment was first utilized to clean the outer surface of BNNT after growth. Supplementary Figure 11b shows the Raman spectrum of Te-BNNT before and after plasma cleaning, and no obvious change was detected. The A_1 and E_2 peaks of Te-BNNT exhibit a clear shift toward high frequency compared with bulk Te, which means that the signal collected is originated from coral Te NW instead of bulk Te cluster attached on BNNT surface. In addition, in the modified device fabrication process, plasma etching with high power density

is required to thinning top layers of the whole length of BNNT, which would also etch away the bulk Te cluster attached on surface.

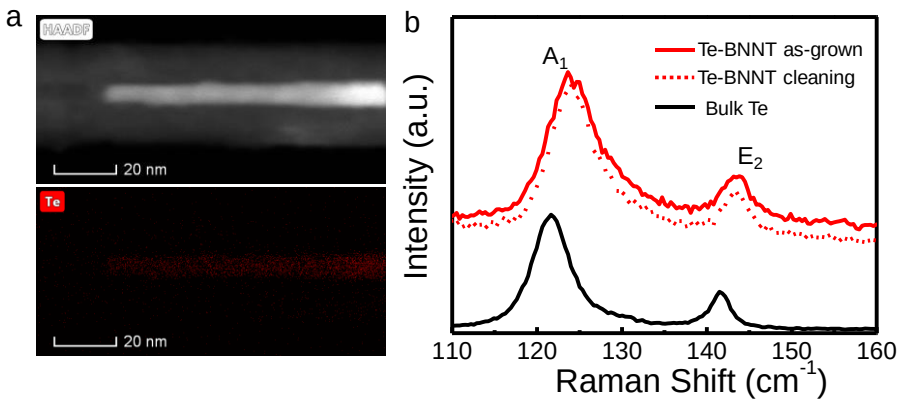

Supplementary Figure 11 | Material characterization of Te-BNNT. a, EDX mapping image of Te-BNNT. **b,** Comparison of Raman spectrum obtained from bulk Te, as-grown Te-BNNT and Te-BNNT after plasma cleaning.

4. Electrical measurements of FET devices based on bare Te NW.

In order to investigate the shielding effect of BNNTs for Te atomic chains, electrical measurements of bare Te nanowires (NWs) were also conducted for comparison. Te NWs were obtained by a solution-based process (see detailed in **Methods** section), and they need to be transferred onto a SiO_2/Si substrate for further characterization (Supplementary Figure 12a). The Te NWs are highly crystallized with diameter ranging from 4 nm to 50 nm as confirmed by AFM and HRTEM (Supplementary Figure 12b and 12c).

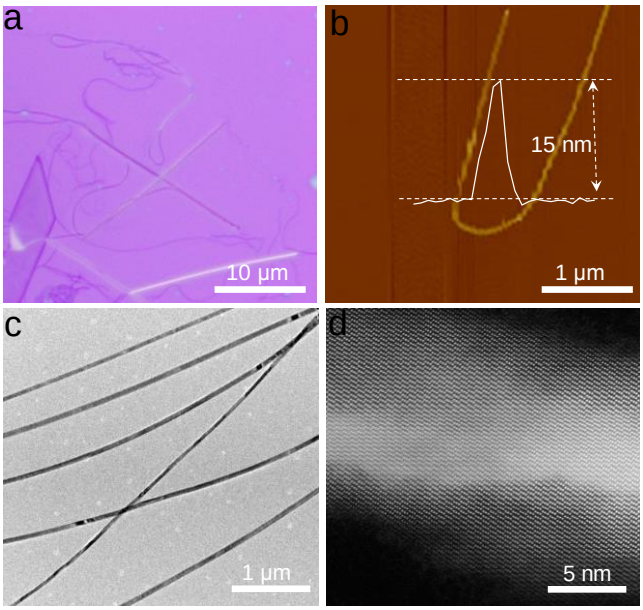

Supplementary Figure 12 | Characterization of solution synthesized Te NWs. a, Optical microscopy and **b,** corresponding AFM height profile of bare Te NW. **c,** Low magnitude TEM and **d,** HRTEM image of a Te NW.

Supplementary Figure 13a and 13b present the electrical performance of a 13-nm-diameter Te NW FET with a channel length of 100 nm measured at room temperature. The device exhibits the typical p-type characteristics with on/off ratio on the order of ~1×10^2 due to distinct short-channel effects and narrow bandgap of Te. The drain current can reach over 900 mA/mm due to the high hole mobility of Te.

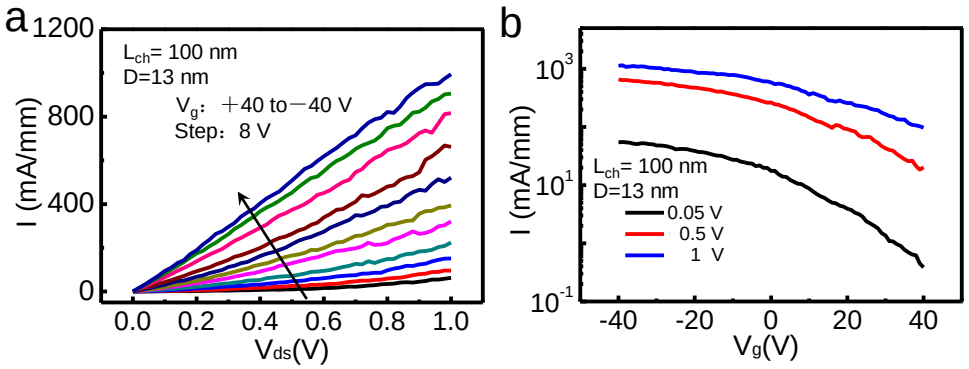

Supplementary Figure 13 | Electrical performance of a Te NW transistor. a, output curves and **b,** transfer curves of the device with a short channel of 100 nm.

The current capacity of solution synthesized Te NWs was studied based on 100 nm

channel devices. As shown in Supplementary Figure 14, the average value for bare Te NWs is estimated be 7.6×10^{6} A cm^{-2}, while the maximum ampacity value for the Te-BNNTs can be significantly improved up to 1.5×10^{8} A cm^{-2}, almost two orders of magnitude larger than the bare ones.

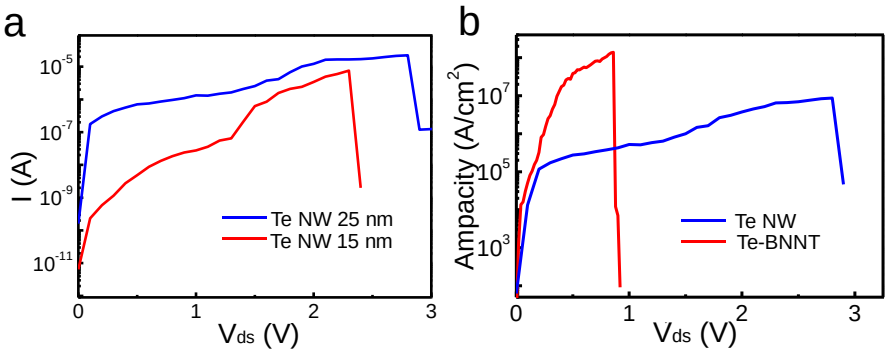

Supplementary Figure 14 | I-V curves up to breakdown of devices. a, Te NW devices with different diameters. **b,** Te NW and Te-BNNT devices with the same diameter.

The diameter-dependence on/off ratio and maximum drain current based on long-channel Te NW devices are presented in Supplementary Figure 15, where the data are elucidated from more than thirty bare Te NW devices. Due to the enhanced gate electrostatic control in narrow nanowires, the on/off ratio increased sharply from $\sim1\times10^{2}$ to $\sim1\times10^{5}$ as the diameter decreases from 40 to 6 nm. However, the narrower samples exhibit the opposite tendency with smaller current density since they are more susceptible to surface oxidation and electrical defects. Indeed, FETs based on ultra-narrow Te NWs (less than 6 nm) cannot sustain electrical conduction and gate modulation since the crystalline structure of Te NW cannot be preserved well during fabrication and measurements in ambient.

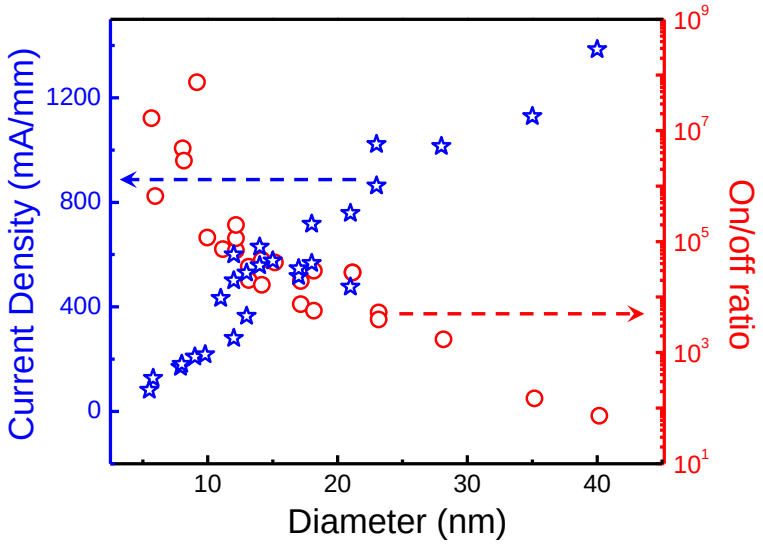

Supplementary Figure 15 | Diameter-dependent electrical performance of Te NW transistors.

5. Thermal stability and electrical properties of Te-BNNTs.

In-situ temperature-dependent Raman spectroscopy was conducted to investigate the thermal stability of Te-BNNTs and bare Te NWs. The Raman signals were collected after the samples annealed for 5 min in ambient environment. As shown in Supplementary Figure 16, bare Te NWs are easily degraded and damaged at 250 ºC, which is much lower than that for those shielded by BNNTs (400 ºC). The shift of Raman peaks can be attributed to the non-crystalizing phase change induced by high temperatures.

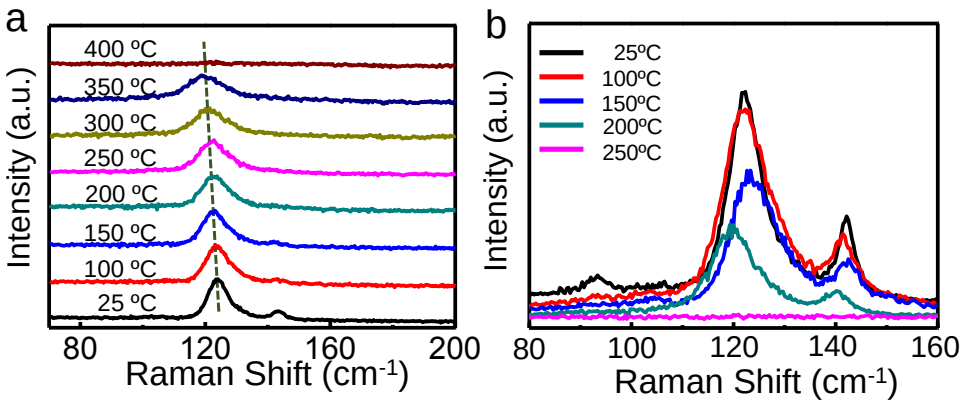

Supplementary Figure 16 | *In-situ* temperature-dependent Raman spectra. a, Te-BNNTs and **b,** bare Te

NWs.

Plasma etching of the BN shielding layer is very sensitive to the etching time. As shown in Supplementary Figure 17, after 30 s of etching, the thickness of BNNT decreases from 27 nm to 16 nm, and the top BN layer could be completely removed, resulting in a Ni/Te contact at interface. The over etching of BN deteriorates the performance of Te-BNNT devices and leads to a smaller breakdown current of 2.3×10^{-6} A, compared with 17.4×10^{-6}A obtained from the device with optimized 20 s etching time.

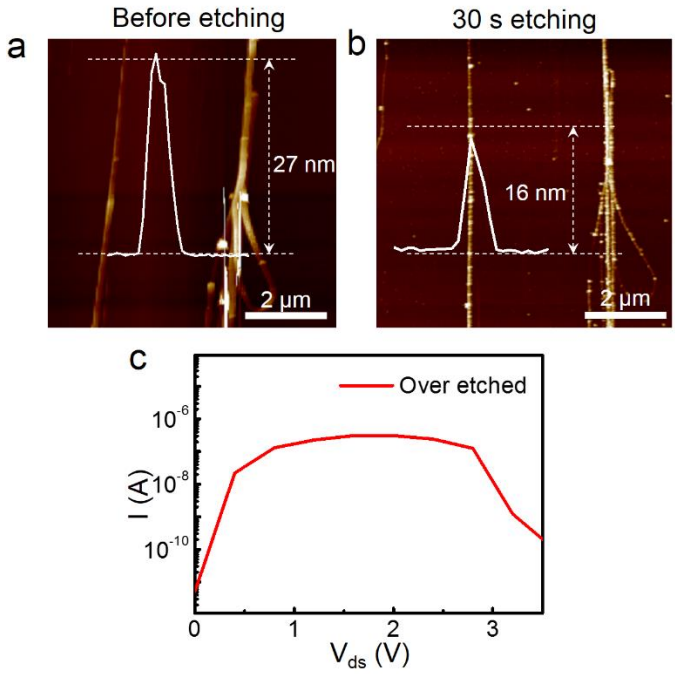

Supplementary Figure 17 | Electrical performance of Te-BNNT devices after plasma etching. **a-b**, AFM height profile of Te-BNNT before and after 30 seconds plasma etching. **c,** I-V curve of a Te-BNNT device after 30 seconds of etching.

The current capacity of semiconducting 1D nanowires were summarized in Supplementary Table 1. This value of 1.5×10^8 A/cm^2 for Te-BNNT exceeds most of the semiconductor NWs, and it is even higher than the most-studied quasi-1D metallic nanowires with high-ampacity (such as $TaSe_3$, $ZrTe_3$). Indeed, it is only slightly smaller than the

semiconducting SWCNTs with the highest value of 3~9 × 10^8 A/cm^2.

Supplementary Table 1 | Comparison of ampacity of devices based on semiconducting nanowires

Semiconductor	L_{ch} (μm)	D (nm)	I_{max} (μA)	Ampacity (MA/cm^2)
Si	5.06	180	170	0.1
PbSe	3	80	10	0.5
Ge	3	20	0.7	0.56
SnO_2	2.2	50	25	1
GaN	3.2	400	3200	3
InP	2	100	1000	10
InAs	1.5	33	96	10
$NiGe_2$	1.6	50	850	35
ZnO	3	228	1000	63
SWCNT	0.02	1.2	10	880
SWCNT	0.3	1.2	3~6	264~528
Te-BNNT	**0.1**	**5**	**29**	**150**

The BNNT shielding of Te NWs enables the FETs to functionalize even with the Te diameter of 2 nm. As shown in Supplementary Figure 18, the FET exhibits p-type transport behaviors, and the on-state current could reach up to 35 mA/mm at V_{ds}=4V. The on/off ratio at drain bias of 1V is over 1×10^2, which is still a decent value considering the short-channel effect, narrow bandgap of ~0.4 eV and Schottky-like large contact resistance. Similar to n-type Te-BNNT FETs, I_{ds} increases exponentially at higher V_{ds}, showing a typical Schottky barrier like characteristics, due to the inserted thin BN layer between Ni and Te.

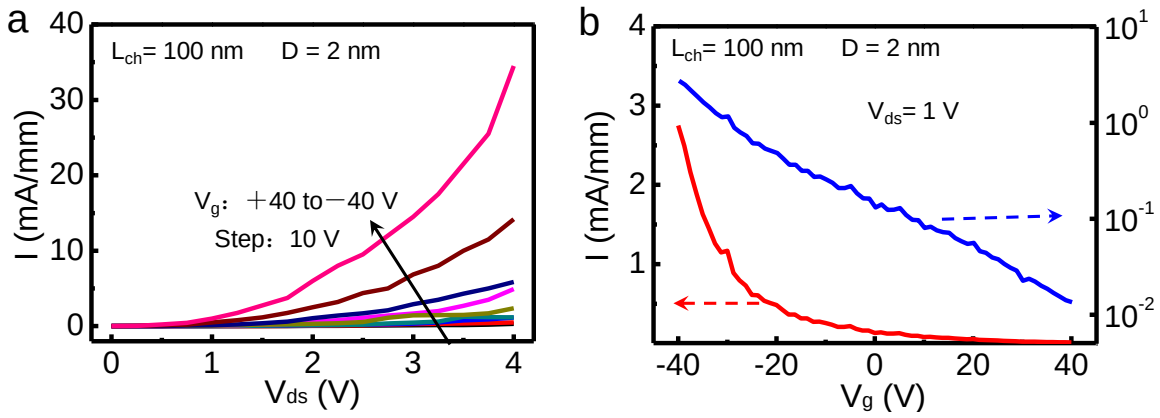

Supplementary Figure 18 | Electrical characteristics of a p-type Te-BNNT transistor with a channel length of 100 nm. a, output curves of the device. **b,** corresponding transfer curves of the same device at V_{ds}=1V.

6. Contact resistance in Te-BNNTs devices.

It is essential to evaluate the channel mobility (μ_{ch}) of Te atomic chains. However, the large contact resistance due to the tunneling resistance of BN layer and general difficult to contact NWs would underestimate the intrinsic mobility (μ) of Te atomic chains. Thus, we need to eliminate the influence of contact resistance (R_c). For FET devices, two techniques can be employed to correct μ. The transfer length measurement (TLM) requires multiple devices of varied L, thus it is only plausible for large-area samples. On the contrary, the Y function method (YFM) can be conducted based on individual devices, which is much more suitable for Te-BNNT FETs with short channel[5,6].

The I_{ds} in linear region could be described as following:

$$I_{ds} = \frac{W}{L} C_{ox} \mu_e (V_{gs} - V_{th}) V_{ds} = \frac{W}{L} C_{ox} \frac{\mu_0}{1 + \theta (V_{gs} - V_{th})} (V_{gs} - V_{th}) V_{ds}$$

The μ_e, μ_0, C_{ox}, V_{th}, W, L, and θ represents the effective mobility in linear regime, the intrinsic mobility, the capacitance between the channel and the gate per unit area, the threshold voltage, the channel width, the channel length, and the mobility attenuation

coefficient, respectively, and the Y-function can be defined as

$$Y - Function = \frac{I_{ds}}{\sqrt{G}} = \sqrt{\frac{WC_{ox}V_{ds}\mu_0}{L}} \cdot (V_{gs} - V_{th})$$

Where the transconductance G could be described by

$$G = \frac{\partial I_{ds}}{\partial V_{gs}} = \frac{WC_{ox}V_{ds}\mu_0}{L} \frac{1}{\left[1 + \theta(V_{gs} - V_{th})\right]^2}$$

Based on the transfer curve at V_{ds}= 0.8 V, we can linear fit the derived quantity Y function in the sublinear regime of on state (Supplementary Figure 19). From the slope of Y-function, we can extrapolate μ_0 value at V_{ds}=0.8V, which is independent of the attenuating factors, was 1.85 $cm^2\ V^{-1}s^{-1}$. The mobility attenuation factor θ can be described as

$$\theta = \theta_{ch} + \theta_c = \theta_{ch} + \mu_0 C_{ox} R_c \frac{W}{L}$$

where θ_{ch}, θ_c, and R_c denote the mobility attenuation factor from the channel, mobility attenuation factor from the contact and the contact resistance, respectively. Assuming that θ_{ch} is negligible, the value of θ is estimated to be 0.007. The corresponding gate-dependent resistance is plotted in Supplementary Figure 19d, $2R_c$ at high V_g was estimated to be 12 KΩ · μm. This value is much higher than widely studied metal/2D systems, which is supposed to be introduced by the inserted BN layer.

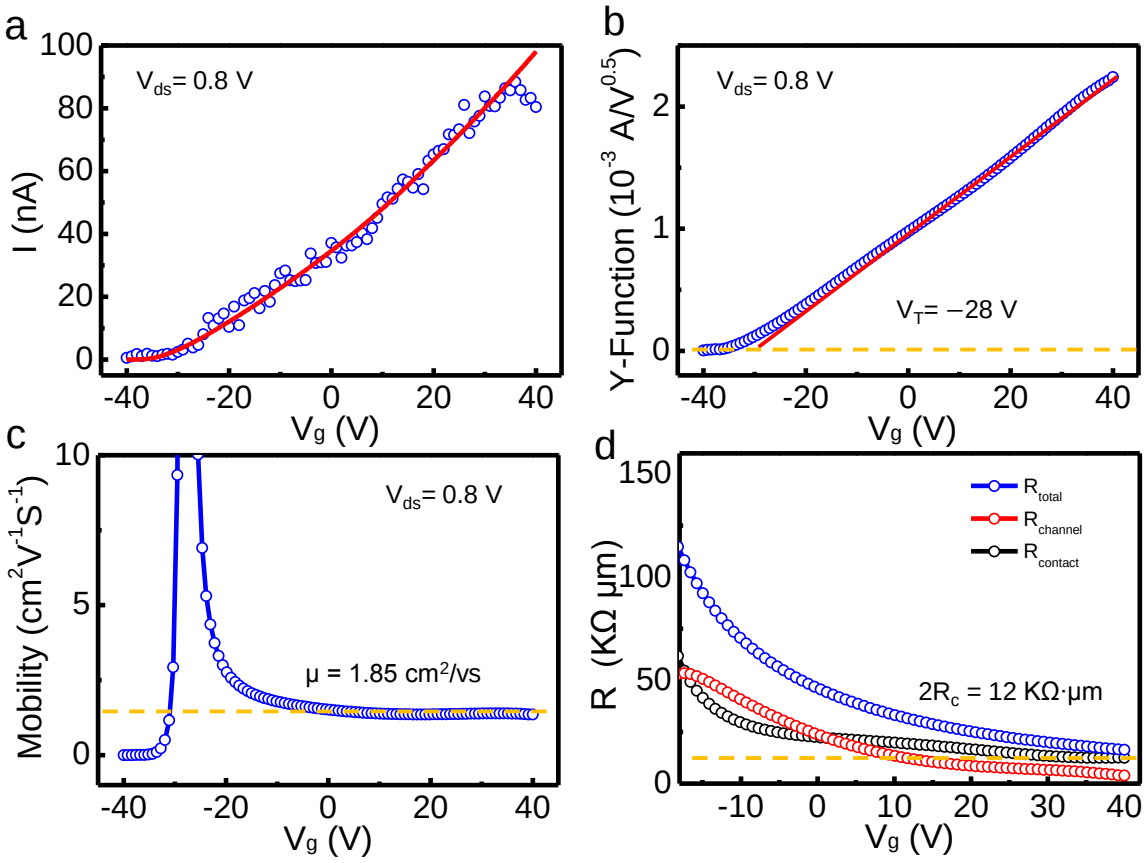

Supplementary Figure 19 | Estimation of carrier mobility and contact resistance using Y-function method. a, The transfer curve of a FET with 2 nm Te atomic chains as the conducting channel at V_{ds}=0.8 V. **b,** Y-function plots of the device. **c,** The calculated intrinsic carrier mobility of the Te atomic chains. **d,** The gate dependent resistance of the device.

Reference

1. Andharia, E. *et al*. Exfoliation Energy, Quasiparticle Band Structure, and Excitonic Properties of Selenium and Tellurium Atomic Chains. *Phys. Rev. B* **98**, 035420 (2018).
2. Giannozzi, P. *et al.* QUANTUM ESPRESSO: a Modular and Open-Source Software Project for Quantum Simulations of Materials. *J. Phys. Condens. Matte*. **21**, 395502 (2009).
3. Perdew, J.P., Burke, K. & Ernzerhof, M. Generalized Gradient Approximation Made Simple. *Phys. Rev. Lett*. **77**, 3865 (1996).
4. Lee, C.H., Xie, M., Kayastha, V., Wang, J. & Yap, Y.K. Patterned Growth of Boron Nitride Nanotubes by Catalytic Chemical Vapor Deposition. *Chem. Mater.* **22**, 1782–1787 (2010).
5. Li, S.L. et al. Thickness-dependent interfacial coulomb scattering in atomically thin field-effect transistors. *Nano lett*. **13,** 3546–3552 (2013).

6. Kim, T.Y. *et al.* Electrical properties of synthesized large-area MoS_2 field-effect transistors fabricated with inkjet-printed contacts. *ACS Nano* **10,** 2819–2826 (2016).